

Polarization Demosaicking for Monochrome and Color Polarization Focal Plane Arrays

Simeng Qiu, Qiang Fu, Congli Wang, Wolfgang Heidrich

King Abdullah University of Science and Technology (KAUST), Saudi Arabia

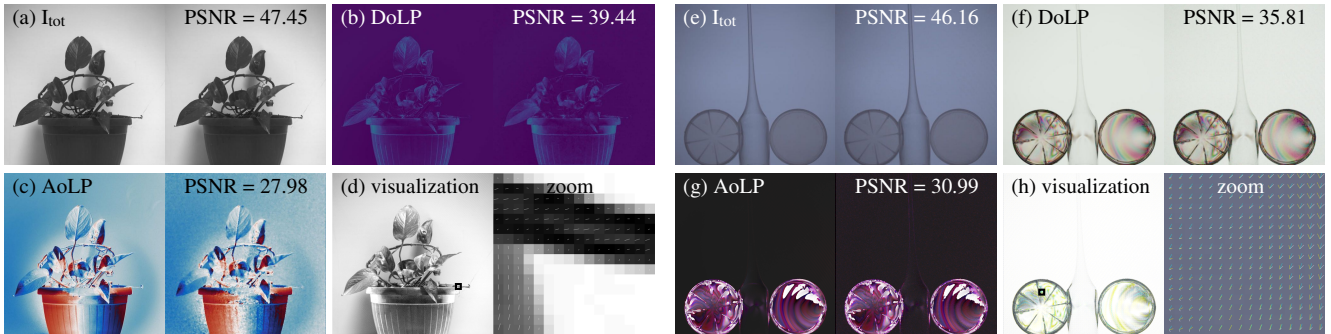


Figure 1: Left (a)-(d): Monochrome polarization demosaicking results for total intensity, DoLP, AoLP and visualization with unpolarized illumination. Right (e)-(h): Color polarization demosaicking results for total intensity, DoLP, AoLP and visualization with polarized illumination. Our proposed algorithm outperforms state of the art for both monochrome and color polarization focal plane arrays.

Abstract

Division-of-focal-plane (DoFP) polarization image sensors allow for snapshot imaging of linear polarization effects with inexpensive and straightforward setups. However, conventional interpolation based image reconstruction methods for such sensors produce unreliable and noisy estimates of quantities such as degree of linear polarization (DoLP) or angle of linear polarization (AoLP). In this paper, we propose a polarization demosaicking algorithm by inverting the polarization image formation model for both monochrome and color DoFP cameras. Compared to previous interpolation methods, our approach can significantly reduce noise induced artifacts and drastically increase the accuracy in estimating polarization states. We evaluate and demonstrate the performance of the methods on a new high-resolution color polarization dataset. Simulation and experimental results show that the proposed reconstruction and analysis tools offer an effective solution to polarization imaging.

CCS Concepts

- Computing methodologies → Computational photography;

1. Introduction

Polarization is an important property of light in addition to its amplitude and phase. Polarization imaging has found uses in various disciplines and applications such as inspection of objects to detect stress, scratch recognition, transparent objects shape detection when the low-contrast environment appears. For future perspectives, it can be applied in microscopy to 3D image reconstruction and ranging from remote sensing. In nature, many diverse species have polarization sensitive vision systems, e.g., honeybees, mantis shrimps, cephalopods, etc. [Hor14]. Unfortunately, human beings are incapable of discerning polarization effects with the naked eye.

To facilitate polarization in our daily life, a variety of polarization imaging, a.k.a imaging polarimetry techniques have been developed with the aid of various polarizing optical elements over the past few decades [TGCS06, AK02]. Nonetheless, high-resolution snapshot polarization imaging remains a significant challenge.

Recently a class of division-of-focal-plane (DoFP) image sensors have been developed, featuring compactness, non-moving parts, and a snapshot capture mode. In such cameras, a micro-polarizer array with four polarization measurements is integrated into the pixels of the focal plane array sensor, similar to the way Bayer filters are integrated into color cameras [YMU^{*}16, GEM^{*}17,

GDB^{*}18, HMB^{*}14]. Both monochrome and color versions of such DoFP polarization cameras are now commercially available. However, effective polarization reconstruction for such sensors remains a largely uninvestigated problem. As pointed out by Tibbs et al. [TDBR17, TDRB18], noise in the measurement may lead to significant artifacts or even incorrect conclusions. We show a simple example in Fig. 2 (b), where Gaussian noise with a standard deviation of 2 out of 255 is added in the measurement, and apparent artifacts arise on the edges in the Degree of Linear Polarization (DoLP) estimation by bilinear interpolation. This problem is even more severe for a color polarization camera since both polarization and color demosaicing should be taken into account.

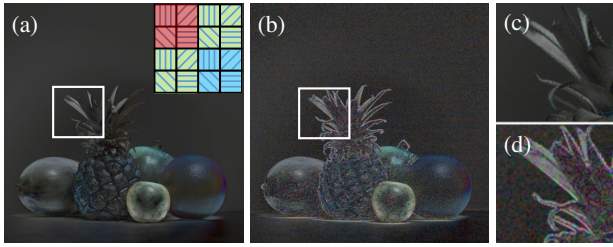


Figure 2: Noise induced artifacts in DoLP for bilinear interpolation in a color polarization camera. (a) Ground truth DoLP. (b) Reconstructed DoLP corrupted by noise (2 out of 255). The zoom regions (c) and (d) illustrate severe artifacts occurring at the edges using bilinear interpolation. The small figure in (a) is a micro-polarizer and Bayer filter layout for a color polarization camera.

To tackle polarization demosaicing problems, various interpolation methods have been proposed, e.g., bilinear, bicubic, cubic spline interpolation [GG11], Fourier domain demosaicing [TLR09], and Intensity Correlation among Polarization Channels [ZLHC16]. A recent thorough survey [MLB18] for a complete summary. However, existing methods are tailored for monochrome polarization images, and distinct edge artifacts are prominent. Therefore, accurate numerical reconstruction from raw measurements for both monochrome and color polarization cameras other than the interpolation method is a must in practical applications.

In this work, we present a high-quality reconstruction algorithm tailored for both monochrome and color polarization images. We propose a comprehensive image formation model by taking into account the Stokes vector conversion, micro-polarizer mosaicing, and noise model. We obtain significantly improved estimates of the intensity, Degree of Linear Polarization (DoLP), and Angle of Linear Polarization (AoLP) for monochromatic and color polarization images by solving an inverse problem within the alternating direction method of multipliers (ADMM) framework. Considering a high-quality large polarization image dataset is lacking in this area, we construct a new dataset with 40 scenes, including both unpolarized and polarized background illumination cases. This carefully captured high-resolution dataset covers a variety of polarization scenarios that are commonly seen in the real world, and we make it public for future research at [DOI:10.25781/KAUST-2VA2X](https://doi.org/10.25781/KAUST-2VA2X). We demonstrate and evaluate our algorithm on this dataset and show numerical comparisons against prevalent monochromatic polarization demosaicing methods and a high-resolution color polarization

demosaicing approach. Simulation and experimental results are carried out to show that the proposed reconstruction method offers an effective solution to polarization imaging.

2. Polarization Demosaicing

2.1. Polarization Model

Stokes vector describes the polarization states for incoherent illumination. In the case of linear polarization, we only consider the first three components of the Stokes vector, i.e.,

$$\mathbf{S} = \begin{bmatrix} S_0 \\ S_1 \\ S_2 \end{bmatrix} = \begin{bmatrix} I_{\text{tot}} \\ I_{\text{tot}} \mathcal{P} \cos(2\phi) \\ I_{\text{tot}} \mathcal{P} \sin(2\phi) \end{bmatrix} = \begin{bmatrix} \frac{1}{2}(I_0 + I_{45} + I_{90} + I_{135}) \\ I_0 - I_{90} \\ I_{45} - I_{135} \end{bmatrix}, \quad (1)$$

where I_{tot} is the total intensity, \mathcal{P} is DoLP and ϕ is AoLP. The Stokes parameters S_0 , S_1 , and S_2 are measured by four intensities I_0, I_{45}, I_{90} and I_{135} with linear polarizers oriented at $0^\circ, 45^\circ, 90^\circ$ and 135° respectively. DoLP and AoLP are defined as

$$\mathcal{P} = \frac{\sqrt{S_1^2 + S_2^2}}{S_0}, \quad \phi = \frac{1}{2} \arctan\left(\frac{S_2}{S_1}\right). \quad (2)$$

See Supplementary Material for the background of polarization.

2.2. Image Formation Model

The essential quantities of polarization analysis are I_{tot} , DoLP, and AoLP. Since the Stokes vector as well as the DoLP and AoLP are highly non-linear functions of the raw sensor data, any noise gets amplified in the estimates for DoLP and AoLP. On the other hand, the formulas for the DoLP and AoLP (Eq. (2)) is also non-convex, making it difficult to directly demosaic these channels. Instead, we propose to solve the Stokes vectors by modeling the physical image formation from Stokes to intensity. With a better estimation of the Stokes vector, higher accuracy in DoLP and AoLP can be obtained.

Since the sensor can only measure intensity, which is just the first component of the Stokes vector, the four intensity values can be obtained by selecting the first component in each Stokes vector for $0^\circ, 45^\circ, 90^\circ$ and 135° . The captured image is a mosaic of intensities filtered by the micro-polarizers, and also by Bayer filters in the color case. This can be represented by pixel-wise multiplications by the respective mosaic masks. Therefore, the polarization image formation model can be expressed as

$$\mathbf{y} = \mathbf{BKAs} + \mathbf{n}, \quad (3)$$

where $\mathbf{s} \in \mathbb{R}^{3cN}$ is the vector form of stacked unknown Stokes parameters for each pixel in each color channel c . For monochrome cameras, $c = 1$, and for RGB cameras, $c = 3$. The total number of sensor pixels is N . $\mathbf{A} \in \mathbb{R}^{4cN \times 3cN}$ is a block diagonal matrix that converts the unknown Stokes vectors to measured intensities via Müller matrices of the four micro-polarizers. $\mathbf{K} \in \mathbb{R}^{3cN \times 4cN}$ is a selecting matrix constructed according to the micro-polarizer layout. $\mathbf{B} \in \mathbb{R}^{N \times 3cN}$ is a selection matrix representing the Bayer filter layout. For the monochrome camera, the Bayer filter diminishes, so $\mathbf{B} = \mathbb{I}$ becomes an identity matrix. $\mathbf{n} \in \mathbb{R}^N$ is additive Gaussian noise, and $\mathbf{y} \in \mathbb{R}^N$ is the captured raw data.

2.3. Inverse Problem

To recover the unknown Stokes vectors, we solve the following constrained optimization problem within the ADMM framework.

This framework has been very successful in many image reconstruction tasks, including color image demosaicking [HST^{*}14], especially when combined with sophisticated regularization terms such as a cross-channel prior [HRH^{*}13], or BM3D denoising [DFKE07]. However, our experiments (see Sec. 4) show that many of these regularizers do not significantly improve reconstruction results for polarization images, and can in fact be detrimental to reconstruction quality.

Instead, our proposed polarization demosaicking method takes the simpler form

$$\begin{aligned} \text{minimize}_{\mathbf{s}} \quad & \frac{1}{2} \|\mathbf{y} - \mathbf{BKA}\mathbf{s}\|_2^2 + \lambda_1 h(\mathbf{D}_1\mathbf{s}) + \lambda_2 h(\mathbf{D}_2\mathbf{s}), \\ \text{subject to} \quad & -1 \leq \mathbf{s}_1, \mathbf{s}_2 \leq 1, \\ & 0 \leq \mathbf{s}_0 \leq 2, \\ & |\mathbf{s}_1|, |\mathbf{s}_2| \leq \mathbf{s}_0, \end{aligned} \quad (4)$$

where the second and third terms are Huber penalties on the derivatives of the Stokes vectors. \mathbf{D}_1 is a convolution with the forward-difference kernels for the X and Y directions, which is $\nabla_x = (0, -1, 1)$ and $\nabla_y = (0, -1, 1)^T$. \mathbf{D}_2 is a Laplacian $(0, 1, 0; 1, -3, 0; 0, 0, 1)$, which are the addition of $\nabla_{xx}^2 = (0, 0, 0; 1, -2, 1; 0, 0, 0)$, $\nabla_{yy}^2 = (0, 0, 0; 1, -2, 1; 0, 0, 0)^T$, and $\nabla_{xy}^2 = (0, 0, 0; 0, 1, -1; 0, -1, 1)$. The Huber penalty [Hub64] is

$$h(x) = \begin{cases} \frac{1}{2}x^2, & |x| \leq \delta, \\ \delta\left(|x| - \frac{1}{2}\delta\right), & |x| > \delta. \end{cases} \quad (5)$$

where δ is a parameter that determines the transition points. We adopt Huber penalty here because it overcomes the penalization of small gradients inherent to total variation (TV), and therefore improves the reconstruction of image gradients while still maintaining sharp edges. The constraints in Eq. (4) confine the physically possible ranges of the individual components of the Stokes vector \mathbf{s} : the total intensity \mathbf{s}_0 ranges from 0 to 2, while \mathbf{s}_1 and \mathbf{s}_2 range from from -1 to 1 . Also, the absolute value of \mathbf{s}_1 and \mathbf{s}_2 are always less than or equal to \mathbf{s}_0 . Sensor noise and interpolation artefacts could result in violations of these physical constraints, so that explicit enforcement in the optimization method becomes necessary in order to avoid artefacts in the derived quantities DoLP and AoLP.

Within the ADMM framework, the problem is split into two subproblems and solved separately. We introduce two slack variables $\mathbf{z}_1 = \mathbf{D}_1\mathbf{s}$ and $\mathbf{z}_2 = \mathbf{D}_2\mathbf{s}$. In the \mathbf{s} -problem, we solve

$$\text{minimize}_{\mathbf{s}} \quad \frac{1}{2} \|\mathbf{y} - \mathbf{BKA}\mathbf{s}\|_2^2 + \frac{\rho_1}{2} \|\mathbf{z}_1 - \mathbf{D}_1\mathbf{s}\|_2^2 + \frac{\rho_2}{2} \|\mathbf{z}_2 - \mathbf{D}_2\mathbf{s}\|_2^2, \quad (6)$$

where its analytical solution is

$$\begin{aligned} & (\mathbf{A}^T \mathbf{K}^T \mathbf{B}^T \mathbf{BKA} + \rho_1 \mathbf{D}_1^T \mathbf{D}_1 + \rho_2 \mathbf{D}_2^T \mathbf{D}_2) \mathbf{s}^* \\ &= \mathbf{A}^T \mathbf{K}^T \mathbf{B}^T \mathbf{y} + \rho_1 \mathbf{D}_1^T \mathbf{z}_1 + \rho_2 \mathbf{D}_2^T \mathbf{z}_2, \end{aligned} \quad (7)$$

This can be solved efficiently by a Conjugate Gradient solver.

We solve the \mathbf{z} -problem by a soft-shrinkage operator

$$\mathcal{S}_\delta(w) = \begin{cases} \frac{\rho}{1+\rho}w, & |w| \leq \left(\frac{1+\rho}{\rho}\right)\delta, \\ w - \frac{\delta}{\rho}, & w > \left(\frac{1+\rho}{\rho}\right)\delta, \\ w + \frac{\delta}{\rho}, & w < -\left(\frac{1+\rho}{\rho}\right)\delta. \end{cases} \quad (8)$$

3. Polarization Image Dataset and Visualization

3.1. Dataset

To the best of our knowledge, existing polarization image datasets are monochromatic, and consist of a few scenes [LGFB18, TDRB18]. High-resolution polarization images with color, are lacking for research. Therefore, we construct a polarization image dataset containing 40 carefully calibrated ground truth images with a wide range of scenes. We try to cover as many naturally occurring polarization effects as possible. We capture different scenes with various shapes, materials, and lighting conditions. In particular, polarized illumination is an essential and useful phenomenon in artifact diagnosis and industrial inspection. We include such images by capturing transparent objects in front of a highly polarized monitor. Figure 3 shows a gallery of our polarization image datasets.

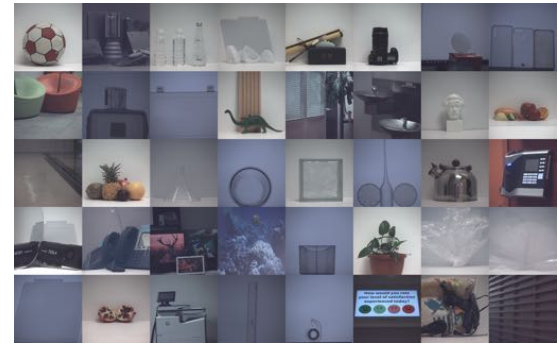


Figure 3: Gallery of our polarization image dataset. Only intensity components are shown here. The complete dataset is available at DOI:10.25781/KAUST-2VA2X.

The dataset is captured by the division-of-time (DoT) strategy. We use a FLIR Grasshopper3 GS3-U3-41C6C color camera. The sensor is a CMOSIS CMV4000-3E5 CMOS, with 2048×2048 pixels. Each pixel is $5.5\mu\text{m} \times 5.5\mu\text{m}$. A Canon EF50mm f/1.8 II lens is used at its maximum aperture size. We mount a linear wire grid polarizer (WP25M-VIS, Thorlabs) on a high-resolution rotary stage (T-RSW60A, Zaber), and place it in front of the camera. The linear polarizer has more than 800 : 1 extinction ratio over the visible spectrum from 420nm to 700nm . For each scene, we capture four groups of raw images at 0° , 45° , 90° and 135° with the same exposure time. Each group has 100 images captured consecutively. We take the average of these 100 images to suppress noise. We also do a 2×2 pixel binning in the averaged image to further increase the signal-to-noise ratio. With such pre-processing, we can generate high-quality ground truth data for I_{tot} , DoLP, and AoLP.

3.2. Visualization

The challenge of visualizing color polarization originates from its 9D high dimensionality. We propose alternative methods in Fig. 1

to complement existing visualization methods for color polarization images. For DoLP, we concatenate the respective DoLPs in its corresponding color channel, and convert it to a color image in the sRGB color space, as shown in Fig. 1 (f). Significant differences in DoLP across color channels lead to color fringes, which reflect certain color channels having larger DoLP values. Such effects can hardly be seen in the corresponding intensity images in Fig. 1 (e).

For AoLPs that are close to 0° or 180° , due to angular wraparound similar angles are assigned vastly different intensities, we propose to take the AoLP in the green channel as a reference, and calculate the absolute difference in blue and red channels with respect to green. We then set the green AoLP values as a transparency α -channel, which is shown in Fig. 1 (g).

Visualizing the polarization state in its entirety is helpful to interpret the 9D polarization states. In analogy to a vector field within a unit circle, the magnitude is the value of DoLP, and the direction represents AoLP. We overlay vector fields on top of the total intensity for 9D visualization, as shown in Fig. 1 (h).

In addition to static visualization, we take advantages of animations to reveal implied information from the underlying polarization states. We synthesize new intensity images with a temporally changing “virtual” polarizer as if the images were taken under the same physical condition, where the virtual linear polarizer can be fully modeled by its Müller matrix. See the Supplementary Material for more details of the above visualization methods.

4. Results

We first evaluate our algorithm by simulation on our polarization image dataset and then by real experiments to demonstrate the real performance. In the simulation, we compare our algorithm against state-of-the-art polarization demosaicking algorithms. The reconstruction quality is evaluated in terms of peak signal-to-noise ratio (PSNR) on three quantities: total intensity, DoLP, and AoLP. In AoLP angle wraparound occurs at 180° , so we first calculate the error between estimated AoLP and ground truth AoLP by

$$\Delta\phi = \min(|\phi - \phi_{\text{ref}}|, 180^\circ - |\phi - \phi_{\text{ref}}|), \quad (9)$$

where ϕ is the estimated AoLP, and ϕ_{ref} is the ground truth. The equation reduces the wraparound confusion.

4.1. Monochromatic Simulation Results

Conventional polarization demosaicking algorithms focus mainly on monochromatic images [MLB18]. State-of-the-art algorithms include bilinear, bicubic, bicubic spline interpolations [GG11], Fourier domain demosaicking [TLR09], and Intensity Correlation among Polarization Channels (ICPC) [ZLHC16]. Therefore, we compare against these methods in the monochrome case. We take the green channel from our color polarization image dataset as the ground truth monochrome polarization data, because it has a better signal to noise ratio than the other two channels.

We show two exemplary results in Fig. 4, a ball scene with unpolarized background illumination and a containers scene with polarized illumination. In both cases, we add Gaussian noise with standard deviation $\sigma = 2$. For conventional methods, there exist distinct edge artifacts because of interpolation, e.g., around the border between black and white patches on the ball. They tend to overestimate DoLP, while our method can suppress these artifacts.

We quantitatively compare PSNRs for all the methods on the intensity, DoLP and AoLP. The results show our method performs significantly better in all the three polarization components.

The latest polarization demosaicking method, ICPC [ZLHC16] claims to achieve better visual results than simpler interpolation methods, and the DoLP and intensity have lower root-mean-square error (RMSE) than bilinear, bicubic, and bicubic spline interpolation. However, running the ICPC method on our full dataset, we observe that although the intensity results of ICPC are almost always better than the other competitors, the DoLP results are not always higher than simple filtering. In particular, for the scenes with polarized illumination the reconstructed DoLP is quite low, as shown in the lower part of Fig. 4. In addition, ICPC does not account for AoLP in the reconstruction, resulting in poor AoLP results. Another competitive method, Fourier domain demosaicking [TLR09] is robust, but the DoLP is sometimes lower than bilinear and ICPC but overall higher than the other methods. The AoLP of Fourier domain demosaicking has the same situation with DoLP. In total, our method has better reconstruction quality.

It is worth noting that the range of DoLP is $[0, 1]$. However, existing methods tend to overestimate DoLP, so in dark regions these methods could have DoLP values larger than 1, which is physically impossible. This has been pointed out by Tibbs et al. [TDRB18]. Our method is more robust to handle such low intensity regions in both unpolarized and polarized illumination cases.

Considering that various factors could affect polarization states, we run the comparison for all the methods on our entire dataset. The average PSNR results are shown in Table 1. This further demonstrates the effectiveness and robustness of our method.

4.2. Color Simulation Results

Since both color and polarization information offers even more information about the scene, our work puts more focus on testing our algorithm on color polarization demosaicking. This brings much more challenges for the interpolation methods, because color and polarization are independent properties of light, and joint demosaicking of the two is difficult to reconstruct in the sense of *interpolation*. There are few algorithms for this purpose in the literature, so instead of comparing with interpolation based methods, we compare different priors/regularizers in our optimization framework.

Specifically, we consider candidate image priors commonly used in image reconstruction, including total variation on first order derivatives (TV), total variation on both first and second order derivatives (TV+2d), Huber loss penalty on first order derivatives (Huber), Huber loss penalty on first and second order derivatives (Huber + 2d), Huber penalty on 1st and 2nd order derivatives combined with BM3D prior [DFKE07] (BM3D), and Huber penalty on 1st and 2nd order derivatives combined with BM3D and cross-channel priors [HRH*13] (BM3D+CC). For the cross-channel prior, we implement it between color channels, as well as between Stokes vector components. We show in Fig. 5 the results for two typical scenarios. The first is a fruit scene with unpolarized indoor illumination (upper part). The second is the cell-phonecases scene with polarized illumination (lower part). In each case, we add Gaussian noise with $\sigma = 2$. Among all the priors, Huber penalty on both first and second order derivatives outperforms the other three candidates for all the polarization components. As the results show, the BM3D prior and cross-channel prior,

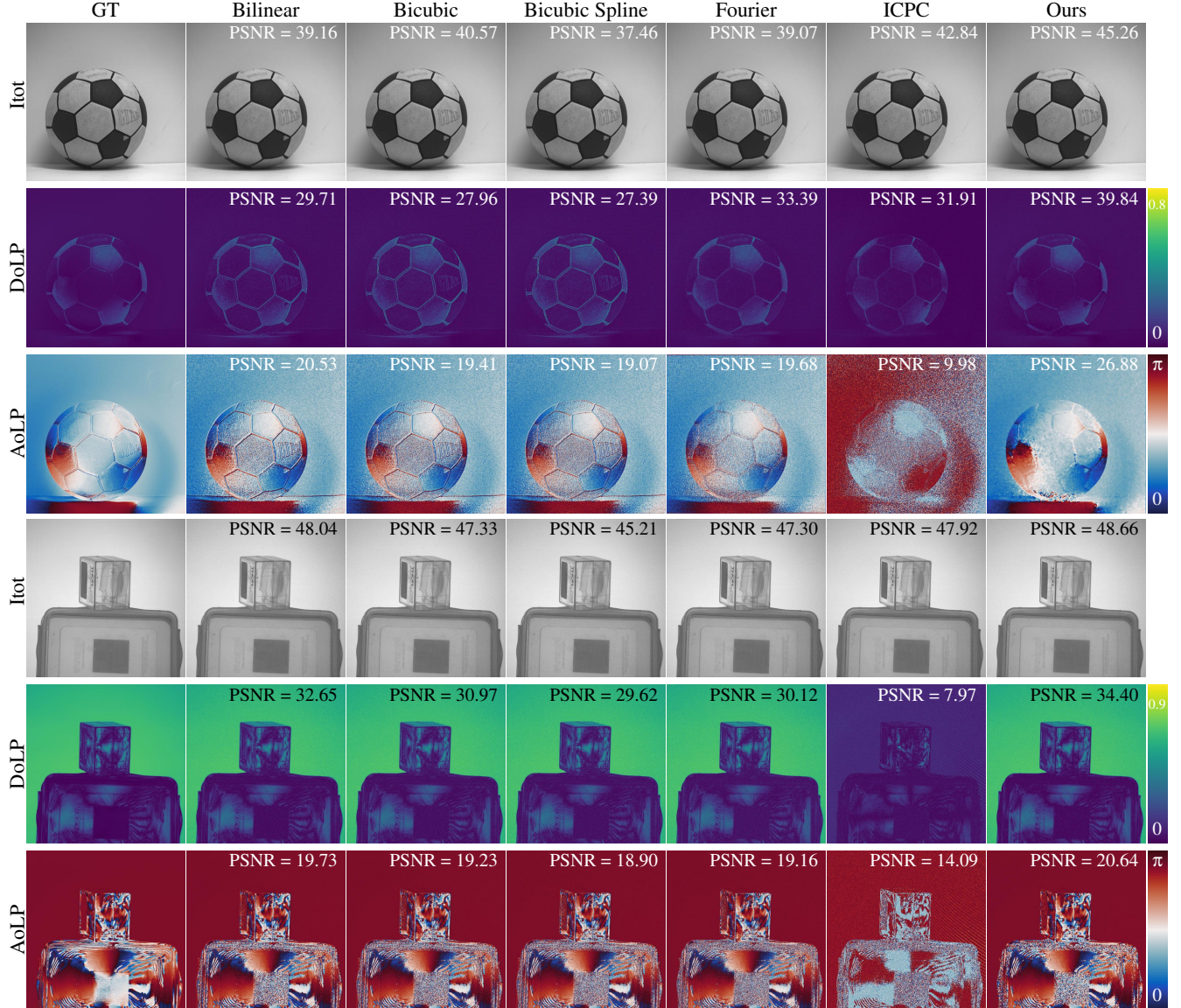


Figure 4: Monochromatic polarization demosaicking on two exemplary scenes in our dataset. The upper part is a ball scene with unpolarized background illumination, and the low part is a containers scene with polarized background illumination. The reconstruction quality is presented in PSNR for all the methods for comparison.

Table 1: Average PSNR results for monochromatic polarization demosaicking ($\sigma = 2$)

| Average PSNR | | Bilinear | Bicubic | Bicubic Spline | Fourier | ICPC | Ours (Huber2d) |
|--------------------------|------|----------|---------|----------------|---------|-------|----------------|
| Unpolarized illumination | Itot | 42.85 | 43.46 | 40.57 | 41.63 | 45.07 | 47.91 |
| | DoLP | 32.45 | 30.71 | 29.94 | 31.64 | 29.38 | 40.43 |
| | AoLP | 19.83 | 18.72 | 18.31 | 18.07 | 10.82 | 25.46 |
| Polarized illumination | Itot | 45.89 | 45.58 | 43.04 | 45.04 | 47.19 | 46.34 |
| | DoLP | 33.99 | 32.92 | 29.53 | 32.38 | 5.42 | 34.63 |
| | AoLP | 30.02 | 29.47 | 28.54 | 29.37 | 15.99 | 31.37 |

which proved to be effective for color images, are not helpful for

color polarization image reconstruction. This indicates that, due to

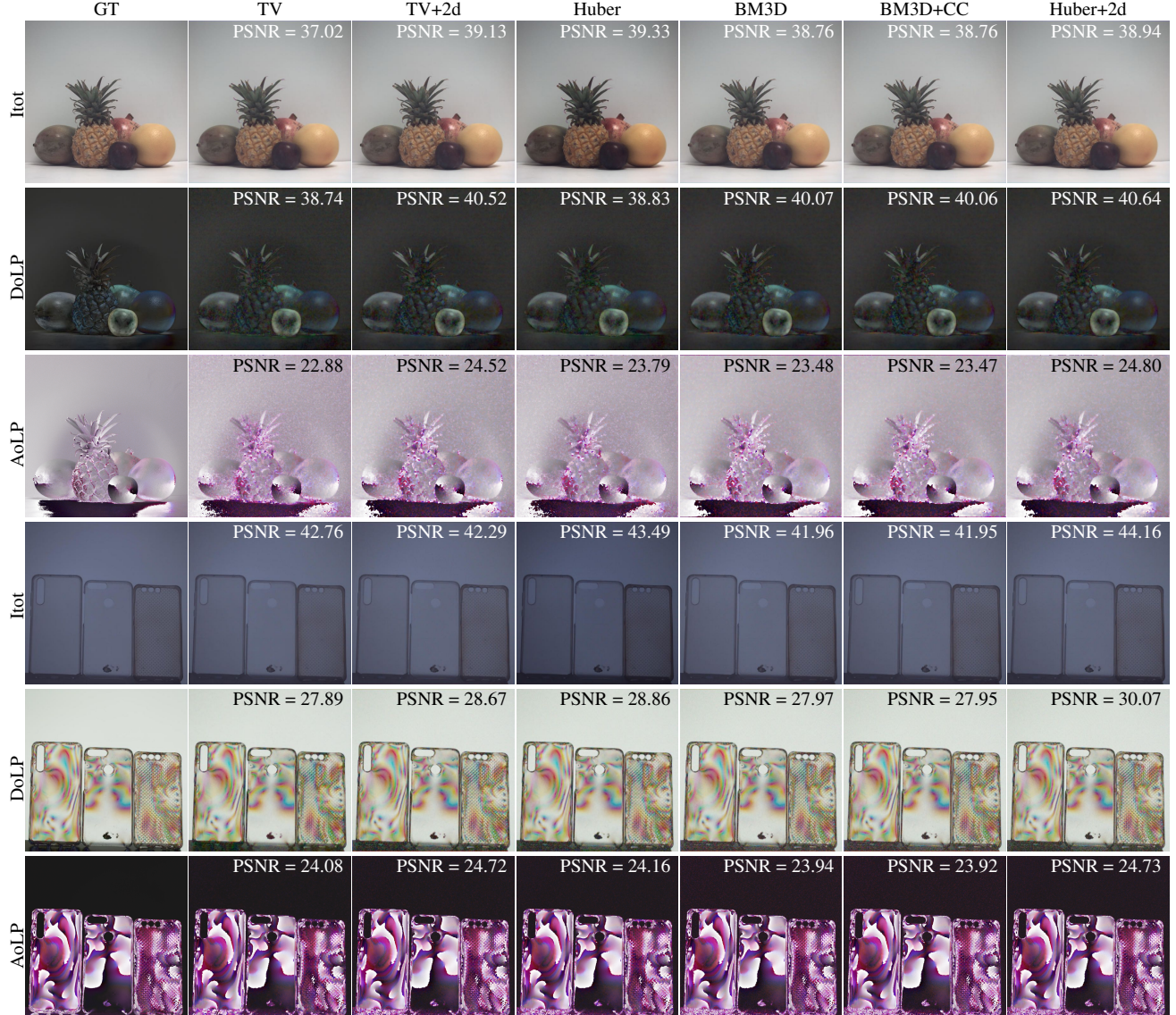


Figure 5: Comparison of optimization based methods with different priors. From left to right are the ground truth (GT) data, TV prior, TV on both 1st and 2nd order derivatives (TV+2d), Huber penalty on 1st derivatives, Huber penalty on both 1st and 2nd order derivatives (Huber+2d), Huber penalty on 1st and 2nd order derivatives combined with BM3D prior (BM3D), and Huber penalty on 1st and 2nd order derivatives combined with BM3D, cross-color channel prior (BM3D+CC). The proposed Huber penalty with 1st and 2nd derivatives outperforms other priors for all the three polarization components.

the very different statistics of Stokes vectors compared with conventional color images, Huber penalty on the first and second order derivatives are the most effective priors for polarization images. We also compared with interpolation methods, and all our optimization based methods have better results than the interpolation method.

In addition, we run our algorithm throughout our dataset. The average PSNR results are shown in Table 2. To consider different noise levels, we compare the result with noise $\sigma = 2$ and $\sigma = 3$ respectively. The results indicate that our proposed method with Huber penalty on both first and second order derivatives works better

than other candidate priors. We also include the results for bilinear interpolation for a baseline comparison. The bilinear interpolation is applied in the four intensity images after color demosaicking. For color demosaicking, we use the Matlab `demosaic` function.

In the monochromatic case, we divide the dataset scenes into two parts according to the illumination conditions. For the two cases, we use different regularization weights for the priors, but we fix the weights for all the images in the same illumination conditions. This is because in the polarized illumination, the brightness of the four captured intensities under the micro-polarizers could drop or

Table 2: Average PSNR results for joint color and polarization demosaicking

| Average PSNR | | Bilinear | TV | Huber | TV2d | Huber2d +BM3D | Huber2d +BM3D+CC | Huber2d |
|---|------|----------|-------|-------|-------|------------------|---------------------|---------|
| Unpolarized illumination $\sigma = 2$ | Itot | 41.52 | 38.39 | 40.28 | 40.32 | 40.01 | 40.02 | 40.18 |
| | DoLP | 31.13 | 32.40 | 37.22 | 34.12 | 37.29 | 37.28 | 37.34 |
| | AoLP | 18.82 | 22.23 | 22.80 | 22.80 | 22.39 | 22.38 | 24.09 |
| Unpolarized illumination $\sigma = 3$ | Itot | 40.77 | 38.01 | 39.73 | 39.48 | 39.80 | 39.82 | 39.97 |
| | DoLP | 29.58 | 33.68 | 36.11 | 33.65 | 36.47 | 36.46 | 37.03 |
| | AoLP | 17.36 | 20.32 | 21.51 | 21.35 | 21.41 | 21.40 | 22.85 |
| Polarized illumination $\sigma = 2$ | Itot | 44.22 | 44.18 | 43.14 | 44.51 | 42.75 | 42.73 | 44.82 |
| | DoLP | 32.68 | 32.50 | 32.15 | 32.74 | 31.02 | 30.99 | 33.64 |
| | AoLP | 30.24 | 30.30 | 31.00 | 29.99 | 28.41 | 28.39 | 31.05 |
| Polarized illumination $\sigma = 3$ | Itot | 43.13 | 43.02 | 41.74 | 43.31 | 41.76 | 41.75 | 43.22 |
| | DoLP | 31.14 | 31.62 | 30.93 | 31.67 | 29.68 | 29.67 | 31.75 |
| | AoLP | 29.54 | 29.82 | 30.22 | 29.53 | 27.84 | 27.84 | 30.11 |

increase drastically for orthogonal polarization angles. In the unpolarized illumination, such variation is much less.

For the performance of our framework, we implemented the method in both a Matlab (CPU) and a CUDA (desktop GPU) version. The CPU implementation of the overall computation cost looks high, however, a short convergence with a good starting point is close to the converged result and provides high-resolution quality and shorter runtime. The GPU version takes about 5.5 seconds per frame, but has further potential for optimization.

4.3. Experimental Results

In real experiments, we use a monochrome polarization camera PHX050S-P and a color polarization camera PHX050S-Q from LUCID Vision Labs. Both polarization sensors are shipped with Sony IMX250MYR CMOS with 2048×2448 pixels. Each pixel size is $3.45\mu\text{m} \times 3.45\mu\text{m}$. In the monochrome case, each 2×2 pixels are a group. In the color case, every 4×4 pixels form a super pixel to sample both polarization and color. We use a Canon EF 50mm f/1.8 II lens operating at the maximum aperture for all the results.

Both color calibration and polarization calibration are necessary before processing. We adopt the method proposed by Akkaynak et al. [ATX*14] to calibrate color correction with a Macbeth color checker. To minimize the influence of polarization, we use unpolarized light for illumination. We find that the Macbeth color checker itself exhibits negligible polarization effects. For simplicity, we only apply white balancing for all the results.

Polarization calibration aims at characterizing the conversion matrix from the Stokes vector to intensities for the micro-polarizers in each color channel. Following the calibration method proposed by York and Gruev [YG12], we mount a high extinction ratio linear polarizer (WP25M-VIS, Thorlabs) on a rotary stage (T-RSW60A, Zaber). A white light source (HPLS245, Thorlabs) is first collimated and then enters the linear polarizer. The exiting light becomes linearly polarized in this way. We rotate the linear polarizer to change the incident angle of polarization. The polarization sensor measures the intensities for different rotation angles. We sweep the rotation angles from 0° to 179° with a 1° step. We take 100 images for each angle and average them to suppress noise. We fit

the intensity changing curves and obtain the respective coefficients to construct the conversion matrix.

We show real experimental results in Fig. 6 for both monochrome and color polarization cameras with the proposed optimization method. For each camera, we show two arbitrarily captured scenes. Since our method deals with the color/polarization demosaicking simultaneously in an optimization framework, the edges can be handled more properly. This means our method is more conservative such that we do not “create” artificial polarization effects, especially on the boundaries in the scenes.

5. Discussion and Conclusion

Polarization imaging is an effective analytical tool across many disciplines. An improved resolution of polarization imaging is of interest, especially for analyzing internal stress of glass and plastics that are not detectable from conventional imaging approaches. Another crucial application includes highlighting the imperfections and scratches of transparent objects, especially those fabricated from plastic. In order to improve the reconstruction quality of the color and polarization information, we have demonstrated an effective algorithm to combat imperfect issues by inverting the unknown Stokes vectors from a single captured mosaic image within the ADMM framework. The resulting intensity, DoLP, and AoLP outperforms interpolation based methods, and offer more accurate measurements for the high dimensional color polarization information. Our self-constructed high-resolution color polarization image dataset covers as many polarization scenarios as possible that occur in the natural world, offering a large database for algorithm evaluation and polarization analysis. With the aid of our high-resolution color polarized illumination images, the surface scratches, and internal stress characteristics of the objects are quite distinct. We envision the methods presented in this paper will enable many more applications in machine vision, biomedical imaging, remote sensing, marine science, etc. for both research and industry.

Acknowledgements

This work was supported by King Abdullah University of Science and Technology as part of VCC center baseline funding and an equipment donation from LUCID Vision Labs. We thank Dr. Alex

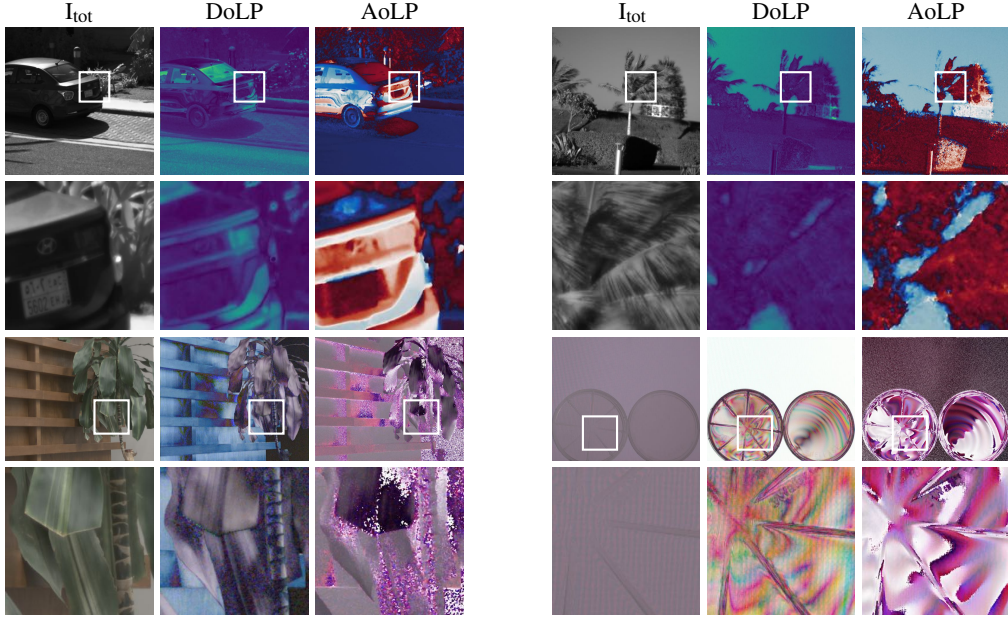


Figure 6: Experimental results for both monochrome (left) and color (right) polarization cameras with the proposed reconstruction algorithm. We show reconstruction results of I_{tot} , DoLP, and AoLP for two arbitrarily captured real scenes.

Tibbs for sharing data for initial test and Nadya Suvorova for helping dataset construction.

References

- [AK02] ANDREOU A. G., KALAYJIAN Z. K.: Polarization imaging: principles and integrated polarimeters. *IEEE Sensors Journal* 2, 6 (2002), 566–576. 1
- [ATX*14] AKKAYNAK D., TREIBITZ T., XIAO B., GÜRKAN U. A., ALLEN J. J., DEMIRCI U., HANLON R. T.: Use of commercial off-the-shelf digital cameras for scientific data acquisition and scene-specific color calibration. *JOSA A* 31, 2 (2014), 312–321. 7
- [DFKE07] DABOV K., FOI A., KATKOVNIK V., EGIAZARIAN K.: Image denoising by sparse 3-D transform-domain collaborative filtering. *IEEE Transactions on image processing* 16, 8 (2007), 2080–2095. 3, 4
- [GDB*18] GARCIA M., DAVIS T., BLAIR S., CUI N., GRUEV V.: Bioinspired polarization imager with high dynamic range. *Optica* 5, 10 (2018), 1240–1246. 1
- [GEM*17] GARCIA M., EDMISTON C., MARINOV R., VAIL A., GRUEV V.: Bio-inspired color-polarization imager for real-time in situ imaging. *Optica* 4, 10 (2017), 1263–1271. 1
- [GG11] GAO S., GRUEV V.: Bilinear and bicubic interpolation methods for division of focal plane polarimeters. *Opt. Express* 19, 27 (2011), 26161–26173. 2, 4
- [HMB*14] HSU W.-L., MYHRE G., BALAKRISHNAN K., BROCK N., IBN-ELHAJ M., PAU S.: Full-strokes imaging polarimeter using an array of elliptical polarizer. *Opt. Express* 22, 3 (2014), 3063–3074. 1
- [Hor14] HORVÁTH G.: *Polarized light and polarization vision in animal sciences*, vol. 2. Springer, 2014. 1
- [HRH*13] HEIDE F., ROUF M., HULLIN M. B., LABITZKE B., HEIDRICH W., KOLB A.: High-quality computational imaging through simple lenses. *ACM Transactions on Graphics (TOG)* 32, 5 (2013), 149. 3, 4
- [HST*14] HEIDE F., STEINBERGER M., TSAI Y.-T., ROUF M., PAJAK D., REDDY D., GALLO O., LIU J., HEIDRICH W., EGIAZARIAN K., ET AL.: FlexISP: A flexible camera image processing framework. *ACM Transactions on Graphics (TOG)* 33, 6 (2014), 231. 3
- [Hub64] HUBER P. J.: Robust estimation of a location parameter. *Ann. Math. Statist.* 35, 1 (1964), 73–101. 3
- [LGFB18] LAPRAY P.-J., GENDRE L., FOULONNEAU A., BIGUÉ L.: Database of polarimetric and multispectral images in the visible and nir regions. In *Unconventional Optical Imaging* (2018), vol. 10677, SPIE, p. 1067738. 3
- [MLB18] MIHOUBI S., LAPRAY P.-J., BIGUÉ L.: Survey of demosaicing methods for polarization filter array images. *Sensors* 18, 11 (2018), 3688. 2, 4
- [TDBR17] TIBBS A., DALY I., BULL D., ROBERTS N.: Noise creates polarization artefacts. *Bioinspiration & biomimetics* 13, 1 (2017), 015005. 2
- [TDRB18] TIBBS A. B., DALY I. M., ROBERTS N. W., BULL D. R.: Denoising imaging polarimetry by adapted BM3D method. *JOSA A* 35, 4 (2018), 690–701. 2, 3, 4
- [TGCS06] TYO J. S., GOLDSTEIN D. L., CHENAULT D. B., SHAW J. A.: Review of passive imaging polarimetry for remote sensing applications. *Appl. Opt.* 45, 22 (2006), 5453–5469. 1
- [TLR09] TYO J. S., LACASSE C. F., RATLIFF B. M.: Total elimination of sampling errors in polarization imagery obtained with integrated microgrid polarimeters. *Opt. Lett* 34, 20 (2009), 3187–3189. 2, 4
- [YG12] YORK T., GRUEV V.: Characterization of a visible spectrum division-of-focal-plane polarimeter. *Appl. Opt.* 51, 22 (2012), 5392–5400. 7
- [YMU*16] YAMAZAKI T., MARUYAMA Y., UESAKA Y., NAKAMURA M., MATOBA Y., TERADA T., KOMORI K., OHBA Y., ARAKAWA S., HIRASAWA Y., ET AL.: Four-directional pixel-wise polarization CMOS image sensor using air-gap wire grid on 2.5- μ m back-illuminated pixels. In *IEEE International Electron Devices Meeting (IEDM)* (2016), IEEE, pp. 8–7. 1
- [ZLHC16] ZHANG J., LUO H., HUI B., CHANG Z.: Image interpolation for division of focal plane polarimeters with intensity correlation. *Opt. Express* 24, 18 (2016), 20799–20807. 2, 4